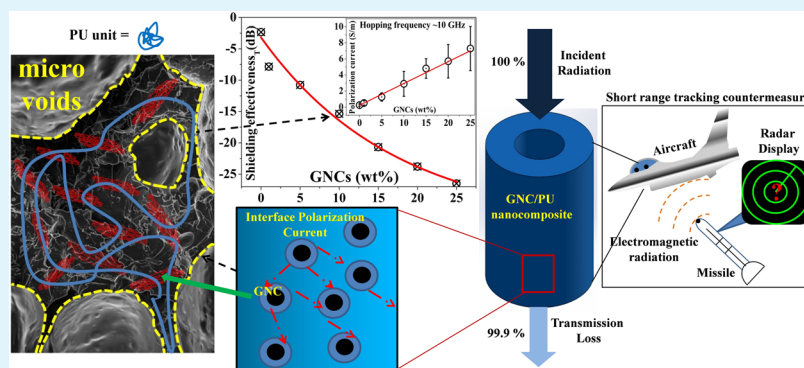# Impressive Transmission Mode Electromagnetic Interference Shielding Parameters of Graphene-like Nanocarbon/Polyurethane Nanocomposites for Short Range Tracking Countermeasures

Arvind Kumar and Prashant S. Alegaonkar*

Department of Applied Physics, Defence Institute of Advanced Technology (DU), Pune 411025, India

Ⓢ *Supporting Information*

ABSTRACT: Shielding the microwave signature (8.2−12.4 GHz, X-band) of a *locked in* target is a tactically important electronic countermeasure. Herein, we report on mitigation in X-band transmission mode shielding parameters for polyurethane (PU), after incorporating graphene-like nanocarbon sheets (GNCs). Initially, PU and variable weight percent (1−25) GNCs/PU paste samples were subjected to Fourier transform infrared, Raman spectroscopy, and scanning electron microscopy. These samples were molded into toroidal shaped specimens by adiabatic hot-pressing technique, for microwave scattering measurements. Parameters, such as complex permittivity ($\epsilon' - j\epsilon''$), alternating current (ac) conductivity, skin thickness, transmission (S_{21}), effective transmission loss (SE_T), and shielding effectiveness were determined, in addition to direct current (dc) conductivity. The real and imaginary components are increased, respectively, by ∼5 and ∼30 times, whereas loss tangent, by ∼7, at 25 wt % loading of GNCs. The ac conductivity is enhanced from 0.248 (PU) to 7.288 S/m (25 wt %) by maximizing transmission loss to −26.45 dB (99.9%) and minimizing thickness to 1−2 mm. The dc percolation threshold is found to be low at ∼5 wt %, indicating superior dispersibility of GNCs, thereafter. In analysis, the atomic polarization (at ∼10 GHz) associated with the aromatic urethane amide rings acts as a backbone to engage incident electromagnetic field wiggles. The coupling occurs via charge transfer polarization currents at doubly bonded nitrogen, oxygen, and hydrosorbed sp^3 carbon sites in GNCs. The field−matter interaction is dominant at the microvoid skin interface between GNCs and PU. Possible polarization mechanism is explained. The GNCs/PU nanocomposites are realized as an effective electromagnetic interference shielding block in the tracking band. The details are presented.

KEYWORDS: *electromagnetic interference shielding, graphene-like nanocarbon, nanocomposites, interface polarization, and transmission loss*
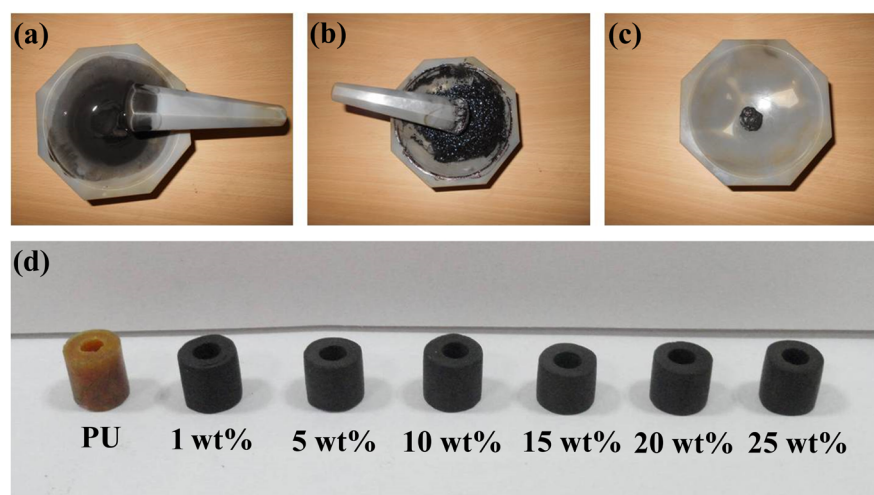
1. INTRODUCTION

Managing the signature of an object at short range tracking (8−12 GHz, X-band) threat from a seeker projectile is of great tactical importance.[1] The signature involves a characteristic combination of geometry, physical optics, and, importantly, reflection properties of the target. The combination, effectively known as the radar cross-section, could be quantified in terms of the shielding effectiveness (SE) of the target. Broadly, SE is the ratio of reflected-to-incident power of radiation, measured in decibels. And the amount of reflection depends on correlation between the wavelength (λ) of the incident signal to the dimension of the target (d). The condition, $d < \lambda$ yields Rayleigh scattering, whereas for $d > \lambda$ diffraction/specular scattering occurs and for $d \sim \lambda$ Mie scattering is more probable.[2] It is difficult to control each component selectively and tunably because of the arbitrary shape and size of the target. However, surface coating with specific magnitudes of complex permittivity and permeability could be a viable option to enhance transmission loss of the incident electromagnetic signals. Such a surface manages to attenuate electric or

Figure 1. (Upper panel) a typical production batch (a) initial phase of the mixture (liquid state), (b) gel-type paste, and (c) thick paste, in the mortar and pestle (mixing and grinding ~3 h to obtain paste). (Lower panel, d) fabricated torroidal shaped specimen (dimensions: i.d., 3 mm; o.d., 7 mm; and height, 6 mm; postproduction edge polishing). Samples were prepared by injection molding of nanocomposite material into the cylindrical die, followed by sealing and simultaneous heat-pressing (at 120 °C; load ~ 100 kg/cm^2), adiabatically, in the hydraulic press (see Supporting Information Figure S3). Extreme left, pristine PU; right, 25 wt % GNCs/PU nanocomposite.

magnetic field at the coating interface with a minimum amount of reflection. The extent to which field interaction exist causes polarization and motion of the mobile charge carriers, within the surface of the skin, and incident energy is mostly consumed in absorption. For such applications, metallic encasings were preferred previously.[3] However, due to their expensive cost, high density, and tendency for corrosion, in recent years, polymer based nanocarbon composites are being considered as a strong alternative. The SE of such hybrid coating, specifically, depends on inherent properties of filler and polymer matrix. The critical components, for fillers, are dimension, carrier mobility, and structural strength, whereas properties such as conductivity, density, design flexibility, and environmental compatibility are essentially important for the host polymer.

Due to their superior properties, nanocarbons such as single walled (SW) and multiwalled (MW) carbon nanotubes (CNTs) and graphene in the form of polymer nanocomposites were reported to be effective shielding materials in the X-band regime.[4−8] For MWCNTs embedded in reactive ethylene terpolymer,[9] poly(methyl methacrylate) (PMMA),[10] and polystyrene (PS),[11] the values of SE have been reported to be respectively 28 (3.2), 40 (10), and 66 dB (20). The numbers in the parentheses indicate the maximum filler loading. Their shield thickness was reported in the range of 2−2.5 mm. For PS[12] and carbon[13] foam decorated with MWCNTs, the values of SE were respectively 20 (7) and 85 dB (0.5) with thickness ~ 2 mm, whereas the SEs had been found to be 30 (25), 17 (20), and 30 dB (15) respectively for polyaniline (PANI),[14] polyurethane (PU),[15] and epoxy,[16] dispersed with SWCNTs. The shielding thickness was variable from the 5 mm to 1 cm range. Since after the discovery of graphene, the focus of several recent investigations has been on graphene/polymer nano-composites based shielding.[17] In this, graphene incorporated in PANI,[14] nitrile butadiene rubber,[18] and epoxy[19] indicated SE to be respectively 35 (33), 57 (10), and 21 dB (8.8) with shielding thickness ~ 5 mm. In poly(vinylidene difluoride) (PVDF),[20] poly(dimethylsiloxane) (PMDS),[21] and PMMA[22] foam in-corporated with graphene, the magnitude of SE had been reported to be respectively 20 (5), 20 (1.8), and 33.3 dB (0.8). Literature is also available on incorporation of other forms of

nanocarbon in various host polymers such as PANI,[23] polypropylene (PP),[24] and acrylonitrile butadiene styrene[10] with SE ranging from 20 to 50 dB obtained at different shielding thicknesses.

Herein we have identified a peculiar interface polarization mechanism between graphene-like nanocarbon sheets (GNCs, 1−25 wt %) and PU to improve electromagnetic shielding properties of PU, in the X-band region. The nature of GNCs bonding with PU has been analyzed using vibration spectros-copy. The microwave scattering measurements have been carried out on torroidal shaped samples to determine complex permittivity ($\epsilon' - j\epsilon''$), alternating current (ac) conductivity, skin thickness, transmission loss, S_{21}, and shielding effectiveness. The scattering analysis is presented in light of chemical bonding, dispersibility, and the morphology of the nano-composites. The polarization mechanism indicated atomic polarization associated with urethane amide rings acts as a backbone to engage incident electromagnetic field wiggles via charge transfer polarization current at doubly bonded nitrogen, oxygen, and hydrosorbed sp^3 carbon sites in GNCs. By and large, for the transmission loss of ~40%, the required PU thickness is more than a centimeter, whereas almost 99.9% loss recorded for a millimeter thick PU, at 25 wt % loading of GNCs. Details are presented.

2. EXPERIMENTAL SECTION

2.1. Starting Materials. GNCs[25] have been used as a typical nanofiller for nanocomposites preparation. The precursor materials such as polyol-8 resin (Ciba-Geigy, Basel, Switzerland) and diphenylmethan-4, 4'-diisocyanat ($C_{15}H_{10}N_2O_2$; MDI, Merck Chem-ical) were used to synthesize PU, along with analytical grade reagent acetone (Alfa Aesar, Hyderabad, India) as the solvent.

2.2. Sample Preparation. For X-band measurements, the specifications of the waveguide were the torroidal shaped samples with inner diameter (i.d.) 3 mm and outer diameter (o.d.) 7 mm. In order to fabricate such samples, a die assembly has been designed and developed. The details of (a) design and fabrication of the die, (b) preparation of the nanocomposite paste, (c) the adiabatic hot-press technique, and (d) cutting and edge polishing protocols have been provided in the Supporting Information. Figure 1 shows (upper panel)
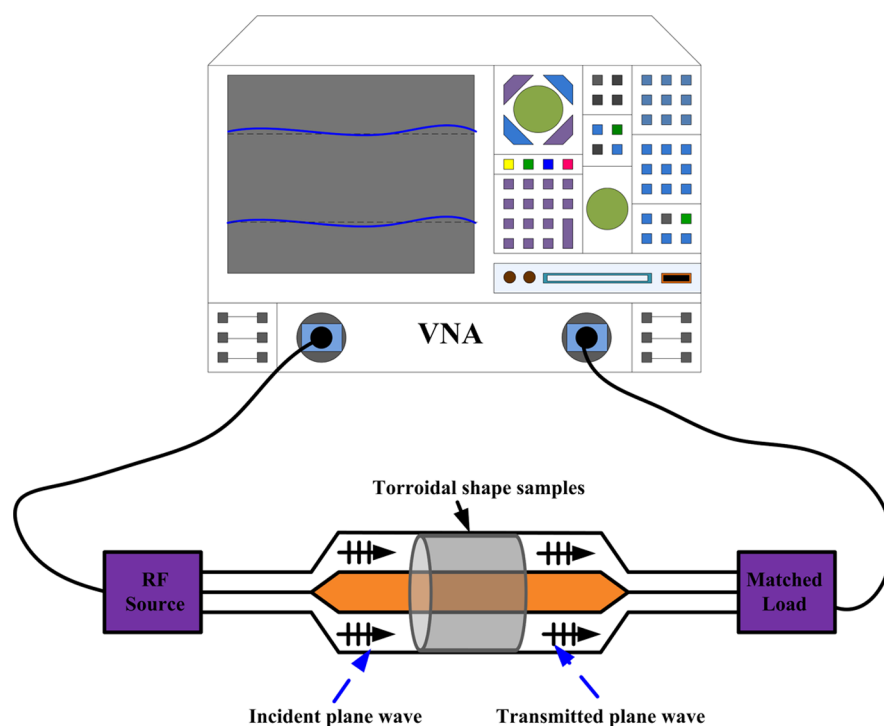
Figure 2. Schematic representation of the electromagnetic scattering measurement setup comprised of the vector network analyzer, a RF source, matched load, and the sample under test in the coaxial transmission waveguide. The frequency range X-band, 8.2−12.4 GHz.

the typical batch processing photograph of nanocomposite paste and (lower panel) fabricated torroidal shape specimens.

2.3. Characterizations and Measurements. *Vibration Spectroscopy.* In order to investigate the nature of the chemical bonding between GNCs and PU, the samples in the paste form were subjected to Fourier transform infrared (FTIR) spectroscopy (PerkinElmer, 1605). Before each scan was performed, background subtraction was carried out for a period of 16 s over the measured range of wavenumber (1000−3000 cm^{-1}). Once the IR detector had been calibrated for the ambient response, one sample at a time was mounted on the platform. Following this, the scan was carried out for a period of 25 s, on the mounted sample. Following this, the measurements were performed on each sample. The resolution of the IR detector was 4 cm^{-1}, for full range.

However, the versatility of IR spectroscopy is limited due to requirements on sample preparation, as well as the detection limit and Raleigh scattering cross-section of the band of interest. Hence, complementary to IR technique, Raman spectroscopy measurements were performed using a LabRAM HR-800 spectrometer. The spectrometer is equipped with a thermoelectrically cooled charged coupled device and capable of collecting spectra over 100−3500 cm^{-1}. In the present study, the excitation radiation source used was a GaAlAs diode laser, having a wavelength of 785 nm and energy of 10 mW on the sample. The measurements were performed at 180° backscattering geometry with respect to the incident beam. For this purpose, the samples have been prepared by dispersing GNCs, and PU in isopropyl alcohol (IPA), independently, whereas torroidal shaped GNCs/PU nanocomposites were fine razor cut and re-dispersed in IPA. The samples, after dispersion, were dropped onto the silicon wafer and dried under IR lamp for a period of 5 min. For measurements, the wafer was mounted on to the workstation stage and a 10× magnification objective of the microscope was focused on the sample to examine the site. With appropriate selection of a spot, the focused laser beam was exposed on the site, at 100× magnification, for a period of 1−3 s to acquire scattering events. In order to confirm the reliability and reproducibility, during the measurements, several such sites have been examined, for each sample. For quantitative analysis, all Raman spectra underwent several chemometric spectral manipulation techniques, using Labspecs 5.0 software from Horiba Industries

Corp., Les Ulis, France. Raleigh and fluorescence induced background scattering have been best fitted for a fourth order polynomial baseline and eliminated from all spectra. A typical batch that underwent the analysis of Raman spectroscopy is shown in the present work.

Direct Current Conductivity. The dc electrical conductivity of PU and a few GNCs/PU composite samples were determined using a standard two-probe method on the coaxial configuration. The data were acquired using a standard Keithley 6487 picoammeter/voltage source equipped with the data acquisition software.

Microwave Measurements. Microwave measurements of the PU and GNCs/PU samples were carried out using a vector network analyzer (VNA, Agilent-E8364B) equipped with the coaxial transmission waveguide (HP broad frequency range coaxial 7 mm air line (85051-60007)) in the frequency range of 8.2−12.4 GHz. Figure 2 shows the schematic representation of the typical electromagnetic shielding measurements setup. Prior to the measurements, VNA was started for 2 h for stabilizing the microwave source. Initially, full two-port calibration of the VNA was performed on the test specimen in order to avoid errors due to directivity, isolation, source match, and load match, etc. The calibration was performed in both forward and reverse directions. The complex permittivity ($\epsilon' - j\epsilon''$) and S_{21} parameters for composites were determined from the measured scattering parameters using the standard Agilent software module 85071, based on the procedure given in the HP product note.[26]

Morphological Measurement. The surface morphology of PU and a few GNCs/PU nanocomposite samples were investigated using a field emission scanning electron microscope (FESEM; Zeiss ΣIGMA) at beam potential of 5 kV. For measurements, the samples were prepared using cryofracture technique. One PU sample at a time was immersed in the liquid nitrogen bath for a period of 5 min. The waiting time allowed the sample to reach the liquid nitrogen temperature. Following this, the sample was taken out and broken instantly. In a similar fashion GNCs/PU nanocomposite samples were fractured. The sample surface was employed to gold coating prior to FESEM imaging. The coating process was carried out using a standard sputtering technique.
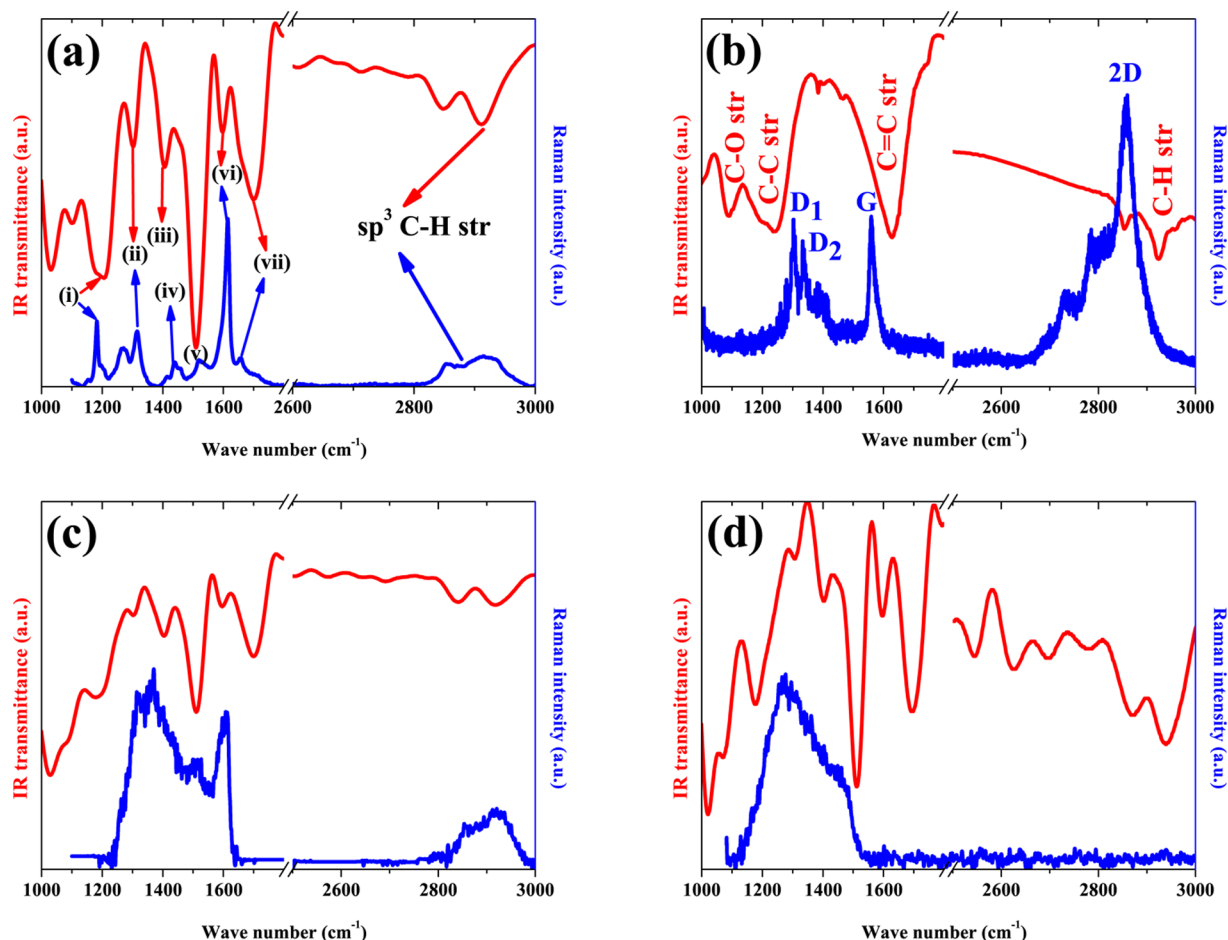
Figure 3. Typical FTIR and Raman spectra (excitation wavelength: 785 nm) recorded for the systems. (a) PU, (b) GNCs, (c) 1 wt %, and (d) 25 wt % GNCs/PU nanocomposite samples. For PU the peak indexing is (i) Urethane amide (Raman active), $\equiv$C−N^{-} (IR), (ii) Urethane amide III (both Raman and IR), (iii) δ(CH) urethane amide III (IR), (iv) δ(CH$_2$) ν_{sym} N$\equiv$C$\equiv$O (Raman), (v) ν (Ar)-urethane amide II ν(C−N) + δ(N−H) (IR), (vi) ν (Ar) (both IR and Raman), and (vii) ν (Ar) urethane amide I ν(C$\equiv$O) (both IR and Raman). The peak positions are indicated in the text.

3. RESULTS AND DISCUSSION

**3.1. FTIR and Raman Spectroscopy: Analysis of Chemical Bonding.** Parts a−d of Figure 3 represent typical FTIR and complementary Raman fingerprints recorded for PU, GNCs, and 1 and 25 wt % GNCs/PU nanocomposite samples, respectively. In Figure 3a, Raman and corresponding IR transmittance bands are assigned for PU. It shows characteristic inelastic vibration modes for urethane amide ($\equiv$C−N^{-}) at ~1184 cm^{-1} and urethane amide III at ~1271 cm^{-1} and δ(CH) for urethane amide III at ~1315 cm^{-1} and δ(CH$_2$) ν_{sym} for N$\equiv$C$\equiv$O at ~1441 cm^{-1}. Correspondingly, the Rayleigh active urethane amide transmittance band is broad and appeared at 1196 cm^{-1}. The amide III and δ(CH) is almost merged at a small band at 1296 cm^{-1}. The prominent IR features at 1515 cm^{-1} are assigned to ν(Ar) of urethane amide II ν(C−N) + δ(N−H), at 1615 cm^{-1} to ν(Ar), and at 1657 cm^{-1} to ν(Ar) urethane amide I ν(C$\equiv$O). The modes appeared between 3000 and 2700 cm^{-1} are a C−H (sp^3 str) band, regardless of the nature of the rest of the PU macromolecule.[27,28] In Figure 3b, the characteristic band at 1088 cm^{-1} indicated the presence of an epoxy (C−O str) group in the pristine GNCs. The bands at ~2925, 1628, and 1300 cm^{-1} are assigned to, respectively, C−H (sp^3 str), C$\equiv$C, and C−C stretching vibrations for GNCs.[27,28] The Raman resonant modes associated with GNCs

are assigned for D-peak (in split form), G-band, and a broad 2D-peak. The details are presented in ref 25. Parts c and d of Figure 3, spectra recorded for respectively 1 and 25 wt % GNCs/PU nanocomposite systems, indicated significant modification with respect to their parent counterparts. In Figure 3c, a broad Raman peak emerged between 1150 and 1400 cm^{-1}, merging all of the active inelastic vibration modes of GNCs as well as PU. However, the band associated with ν(C−N) + δ(N−H) is still existent at ~1511 cm^{-1} for 1 wt % but ceased thereafter with subsequent loading of GNCs, whereas the modes associated with urethane amide, i.e., ν(Ar), backbone of PU, is almost invariant even at low loading of GNCs. However, a significant change in the Raman active C−H str mode is observed for PU after incorporating 1 wt % GNCs. The intensity of this mode is high for GNCs compared with PU, which indicates availability of hydrosorption sites in GNCs. The gradual vanishing trend of C−H str vibrations is consistent even for other wt % samples (profiles not shown here), and in fact the mode practically becomes inactive for 25 wt % GNCs/PU nanocomposites.

The typical trend observed for the transmittance loss of IR bands is in commensuration with the change in Raman active modes for, mostly, all of the samples. Broadly speaking, with subsequent incorporation of GNCs in PU, any change in the band associated amide backbone, i.e., ν(Ar), is marginal. For

these peaks, neither intensity nor vibration frequency is observed to be varied. This preliminarily indicates that the single bonded backbone of the PU matrix mostly remains intact even after incorporation of GNCs. We have summarized our observations as follows: (a) decrease in the Raman peak intensity associated with the nonplanar, hydrogen bonded peaks of urethane amide III $\delta(CH)$ at ~1315 and 1500 cm^{-1} (-N−H-), (b) significant intensity variations in doubly bonded oxygen (C=O at 1700 cm^{-1}), $\delta(CH_2)$ ν_{sym} N=C=O at ~1441 cm^{-1}, nitrogen (=C−N- at 1250 cm^{-1}), and (c) vanishing Raman active sp^3 C−H str modes at ~3000 cm^{-1}. This indicates that hydrogen bonding in the PU matrix is modified heavily after incorporation of GNCs, in addition to a change in the environment at the doubly bonded moieties. Among these, the nitrogen based moieties (-N−H-, N=C=O, and =C−N-) are electron donor loaded species which could be contributing to bonding with GNCs via hydrosorption. In this, the double bonded site could be more reactive, due to π-conjugation, and the effect is, probably, dominant at these sites. In general, the nature of hydrogen bonding is tricky in the sense that neither of these moieties are electronegative nor positive. Thus, the discussions lead to an intermediate conclusion that the nature of the interaction could be hydrosorption in origin, and prone at double bonded sites, dominantly.

3.2. Direct Current Conductivity. Figure 4 shows recorded variations in dc conductivity (σ_{dc}) as a function of
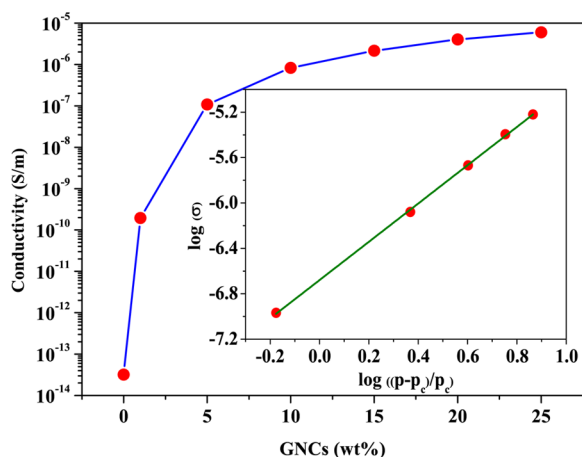
Figure 4. Variations in dc conductivity (σ_{dc}) (in logarithmic scale) as a function of weight fraction (p) of GNCs in the PU matrix. Measurements were performed using a standard two-probe technique, at room temperature. Inset: log−log profile for σ_{dc} vs log$((p - p_c)/p_c)$. The straight line in the inset is fitted using least-squares methods for the obtained data using eq 1 returning the best fit values $p_c \sim 5.0$ wt % and $\gamma = 1.69$ (correlation factor, 0.02).

GNCs weight fraction (p). One can see that, below the weight percent threshold of ~5.0, the conductivity showed a dramatic decrease of ~7 orders of magnitude. This indicates that, above this threshold, the percolating network is formed in the PU matrix. The observed variations could be attributed to the increase in the number of hydrosorped conducting sites. Further, the inset in Figure 4 shows that the electrical conductivity obeys the exponent law.[29]

$$\sigma \propto (p - p_c)^\gamma \tag{1}$$

where σ is the composite conductivity; p, the weight fraction of GNCs; p_c, the percolation threshold; and γ, the critical

exponent. Since the density of GNCs can only be approximately estimated, therefore the weight fraction of GNCs is used instead of volume fraction. For the log(σ) as a function of log$((p - p_c)/p_c)$, the GNCs/PU nanocomposite conductivity agrees well with the percolation behavior as predicted by eq 1. The straight line with $p_c \sim 3.0$ wt % and $\gamma = 1.69$ gives an excellent fit to the obtained data with a correlation factor of 0.02. The percolation threshold is found to be at the lower side, that is, 3.0 wt % GNCs. This could be attributed to efficient dispersibility of GNCs into the PU matrix, thereafter. Theoretical values of γ for a three-dimensional (3D) percolating networks varies from 1.6 to 2.0,[30] while experimental values for carbonaceous materials such as carbon nanotube composites are reported to be varied from 0.7 to 3.1.[31−33]

In a subsequent section analysis of X-band measurements has been presented which resembles discussions presented above.

3.3. Microwave Spectroscopy: Analysis of Scattering Parameters. *Real and Imaginary Parts of Permittivity.* Basically, three mechanisms are responsible for the attenuation of an incident electromagnetic wave; (a) reflection, (b) absorption, and (c) multiple internal reflection losses at the interface due to conductive fillers or porosity of the materials. To begin with, analyzing permittivity response could determine the absorption properties of the test specimens over the measured frequency range.

Parts a and b of Figure 5 are recorded frequency response spectra, respectively, for the real (ϵ') and imaginary (ϵ'') parts of the permittivities for PU and GNCs/PU nanocomposites with variable GNCs weight percent. A systematic increase in both the real and imaginary parts of the permittivity has been observed, over the frequency regime, with the increase in GNCs content.

The response is nearly frequency independent for the real part of permittivity. The flat response showed that PU as well as nanocomposite is a class of non-Debye solid.[34] In general, the frequency dependence of permittivity comes from the polarization mechanism via the Clausis−Mossitte relation. Nevertheless, for all samples small percent variations in the real part of the permittivity (i.e., $\Delta\epsilon'\%$) have been estimated. Differences are estimated at actuals, over the full frequency range. For PU, $\Delta\epsilon'\% \sim 1.03$, whereas, for 5 wt %, $\Delta\epsilon'\% \sim 1.11$, closely resembling to that for PU. As the loading of GNCs increases from 5 to 15 wt %, $\Delta\epsilon'\%$ is found to be saturated to ~16. Thereafter, the percent variation is negative, −3.17 and −15.00, respectively, for 20 and 25 wt % GNCs/PU nanocomposites. The flipping of magnitude of $\Delta\epsilon'$ is indicative of the flip in the operative dipole moment with rapid saturation in both directions.

For the imaginary part, frequency has gradual trendy variations in the measured permittivity loss. However, at higher loadings, small variation is observed for, e.g., in samples 10, 15, and 25 wt %. Thus, both real and imaginary parts of the permittivity are found to be varied, marginally, over the frequency regime.

On a relative scale, the comparison has been made across the categories of the samples by taking an average at logarithmic-normal scale (indicated in Figure 6). At 25 wt %, the value of the real part of permittivity is 9.31 ± 0.03. In contrast, PU offers low (real) permittivity 1.84 ± 0.01. This increase is ~5 times, whereas the imaginary part of permittivity is 1.29 ± 0.03 (for 25 wt %), which indicates an increase by a factor of ~30 with respect to the base value of PU (0.043 ± 0.006). Thus, on
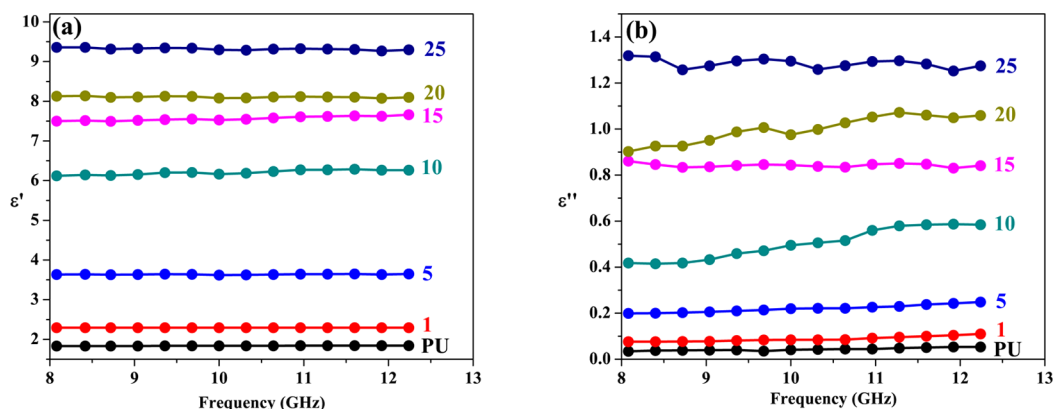
Figure 5. Recorded complex microwave scattering data over the measured frequency regime: (a) real (ϵ') and (b) imaginary (ϵ'') parts of the permittivity spectra for PU and GNCs/PU nanocomposites. The numbers to the right-hand side in each profile indicate the weight percent of the GNCs.
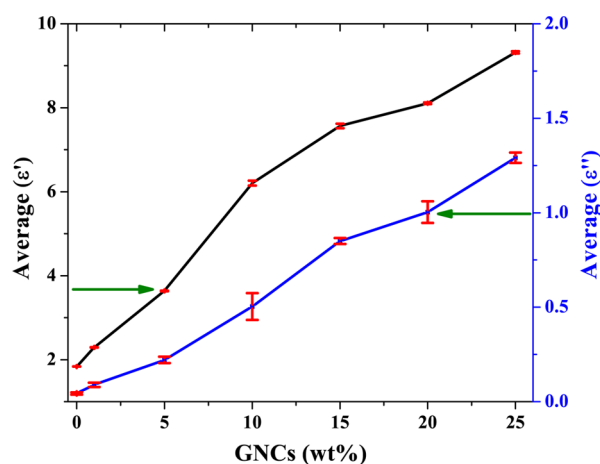
Figure 6. Estimated magnitudes of real ϵ' and imaginary ϵ'' parts of the permittivity (average at logarithmic-normal scale) as a function of GNCs weight percent.

a relative platform, increases in both the real and imaginary parts of the permittivity are due to an increase in ac conductivity via enhancing active modes of charge transfer polarization by GNCs in the PU matrix.

Loss Tangent, Alternating Current Conductivity, and Skin Thickness. The electrical losses inside the nanocomposite material under the test condition could be quantified by the loss tangent (tan δ_e), calculated using tan $\delta_e = \epsilon''/\epsilon'$. The magnitudes of the average tan δ_e (rad) measured for the systems are provided in Table 1. The loss component for PU is 0.024 ± 0.003, whereas for the 25 wt % value it is recorded to be 0.140 ± 0.003. The tan δ_e is increased by a factor of 6. In principal, tan δ_e is the quadrature part of the polarizability vector component in line with the incident electromagnetic field. Its increase indicates greater field losses inside the nanocomposite material. Thus, after incorporating GNCs, in the host matrix, the field losses seem to be increased marginally. Further, using the ϵ'' parameter the ac conductivity (σ_{ac}) of a dielectric material could be evaluated using $\sigma_{ac} = 2\pi f \epsilon_0 \epsilon''$, where, σ_{ac} is measured in siemens per meter, ϵ_0 is the free space permittivity (8.854 × 10^{12} F/m), and f is the applied frequency in hertz. The value of σ_{ac} for PU is 0.248 ± 0.135, which is increased linearly by a factor of 30 times with sequential incorporation of GNCs until 25 wt %. The observed increase is due to donor loaded nitrogen sites such as -N−H-, N=C=O,

Table 1. Magnitudes of Measured Loss Tangent, tan δ_e, and Alternating Current Conductivity, σ_{ac}, for PU and Different Weight Percent GNCs/PU Nanocomposites under Testing[a]

samples	tan δ, rad	σ_{ac}, S/m
PU	0.024 ± 0.003	0.248 ± 0.135
1 wt %	0.039 ± 0.005	0.511 ± 0.255
5 wt %	0.061 ± 0.005	1.261 ± 0.515
10 wt %	0.081 ± 0.011	2.894 ± 1.548
15 wt %	0.110 ± 0.002	4.801 ± 1.215
20 wt %	0.120 ± 0.007	5.706 ± 2.076
25 wt %	0.140 ± 0.003	7.288 ± 2.740

[a]The σ_{ac} is increased linearly by a factor of 30 with subsequent GNCs incorporation up to 25 wt %.

and =C−N- attached to GNCs. The effect seems to be dominant at double bonded GNCs sites, due to π-conjugation with the host matrix.

Further, skin depth is a thickness parameter (δ) to which incident electromagnetic field interacts with the mobile charge carriers to generate charge transfer displacement current in the host medium. This effect is responsible to couple incident field wiggles with charge carriers and a decisively set thickness of the shielding nanocomposite. The magnitude of δ related to σ_{ac} is given by the following relation: $\delta = (1/(\pi f \mu_0 \mu_r \sigma_{ac})^{1/2})$, in which μ_0 is the free space permeability ($4\pi \times 10^{-7}$ H/m) and μ_r is the relative permeability for GNCs/PU nanocomposites, ≈1. Moreover, the skin thickness estimates the distance over which the field intensity decreases to $1/e$ of its original value (0.3678 mW) under the condition $\sigma_{ac} \gg 2\pi f \epsilon_0 \epsilon'$. The estimated values of skin depth in terms of thickness as a function of GNCs weight percent is shown in Figure 8. The magnitude of the skin thickness, δ, for PU is 10.44 ± 2.1 mm, whereas 5.91 ± 1.09 mm is for the 3 wt % GNC. The values are estimated by standard nonlinear regression methods. It shows more than 40% reduction in skin thickness of the sample. Further increase in GNCs weight percent in PU reduced the thickness of shielding to 1.88 ± 0.25 mm (25 wt % GNC). Thus, after the absorption of microwave power, free charge carrier propagation seems to be hindered by reducing the skin thickness. The ability to block charge carrier across the shielding thickness is indicative of higher attenuation microwave power and efficient coupling between field wiggles to the matrix. In a subsequent section, the amount of microwave absorption has been quantified from the scattering data.

Efficient Microwave Absorbing Properties. The mode of measurement is typical transmission measurements (scalar S_{21} measurements). The decibel value describes how much the level of an incident power (or power flux density) has decreased, after passing the specimen under test. The calculation of percentage values presented in Table 2 refers

Table 2. Relationship between Shielding Effectiveness (SE) and Power Transmission (%)

SE, dB	power transmission, %	SE, dB	power transmission, %
0	100	12	6.25
1	81	13	5.00
2	62.80	14	4.00
3	50	15	3.13
4	40	16	2.50
5	31.60	17	2.00
6	25	18	1.56
7	20	19	1.20
8	16	20	1.00
9	12.50	25	0.316
10	10	30	0.1
11	7.90		

to the power relationship. It tells us that at ~20 dB shielding reduced the penetrating power to 1%. To calculate the dB value, the following relation is used to compute SE:

$$SE/dB = 10 \log\left(\frac{P_T}{P_I}\right) \tag{2}$$

where P_I is the incident and P_T the transmitted power.

The scalar S_{21} has been computed, as shown in Figure 7a. The S_{21} is a flat dispersion response, and variations are consistent with the permittivity response. The uniformity of S_{21} indicates that the operative mechanism as explained earlier surmises the obtained results. Further, S_{11} and S_{12} data are not presented; S_{21} alone could not be claimed for the total shielding effectiveness (SE$_{TO}$). For this purpose, SE due to transmission (SE$_T$) has been measured using eq 2 for the effective transmittance loss and plotted in Figure 7b. SE$_T$ is highest for PU and gradually decreased with filler weight fraction. The magnitude of SE$_T$, for PU, is −2.34 dB whereas on the percolation threshold the value has been found to be −10.76

dB. Gradually the value is increased to −26.45 dB for 25 wt % GNCs/PU composites. In general, the trend of SE$_T$ is identical as that of S_{21}. Hence average variation is plotted. For PU the magnitude of SE$_T$ is estimated to be 12 times lower with respect to 25 wt %. Hence, it is interesting to estimate percent variation in transmission loss. Further, the extent of microwave propagation in a medium decides the amount of transmission loss. The discussions on the extent of microwave propagation with percent transmission loss have been presented in a subsequent section.

In the case of polymer (i.e., at low microwave electric conductivity), the values of percent transmission loss obtained for the samples provides an idea of the electromagnetic behavior in the composite material under test. From Figure 8,
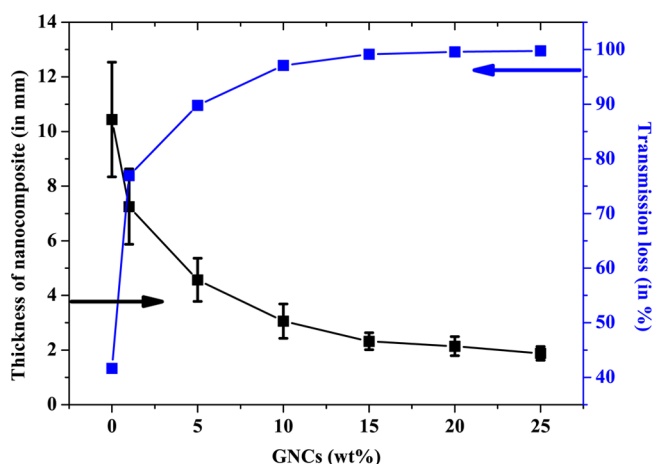
Figure 8. Variation in thickness measured (mm) and transmission loss (%) as a function of weight percent of GNCs in PU. Measurements on base PU are also indicated for comparison.

one can see that ~40% transmission loss requires a thickness > 10 mm for PU, whereas incorporation of GNCs in PU improves the magnitude of the transmission loss. Typically, at optimum percolation threshold that is ~5 wt %, the thickness of the composite is less than 5 mm. With subsequent incorporation of GNCs, for instance, 25 wt %, almost 99% transmission losses have been achieved at thickness ~ 1−2 mm. This indicates that incorporation of GNCs is advantageous due
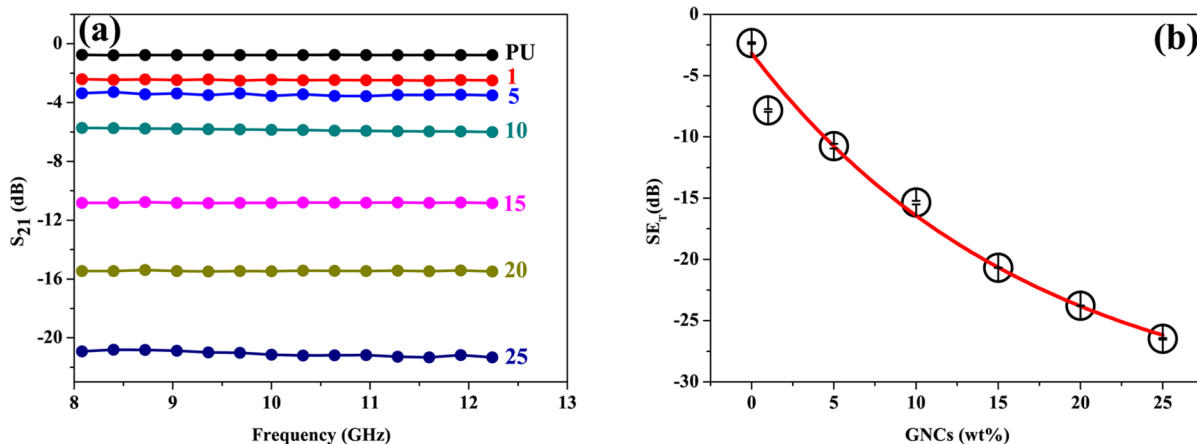

Figure 7. (a) Variation in scalar S_{21} parameters measured in dB unit. Response is plotted over 8.2−12.4 GHz for PU and variable weight percent of GNCs in composite. (b) Computed shielding effectiveness due to transmission loss, SE$_T$.

to its inherent self-functional property generating physicoche-misorption prone interfacial interactions. As a result, one can achieve a high amount of transmission loss at relatively low thicknesses.

Morphological Analysis. Figure 9 shows a typical set of micrographs indicating surface morphology of the cryofractured
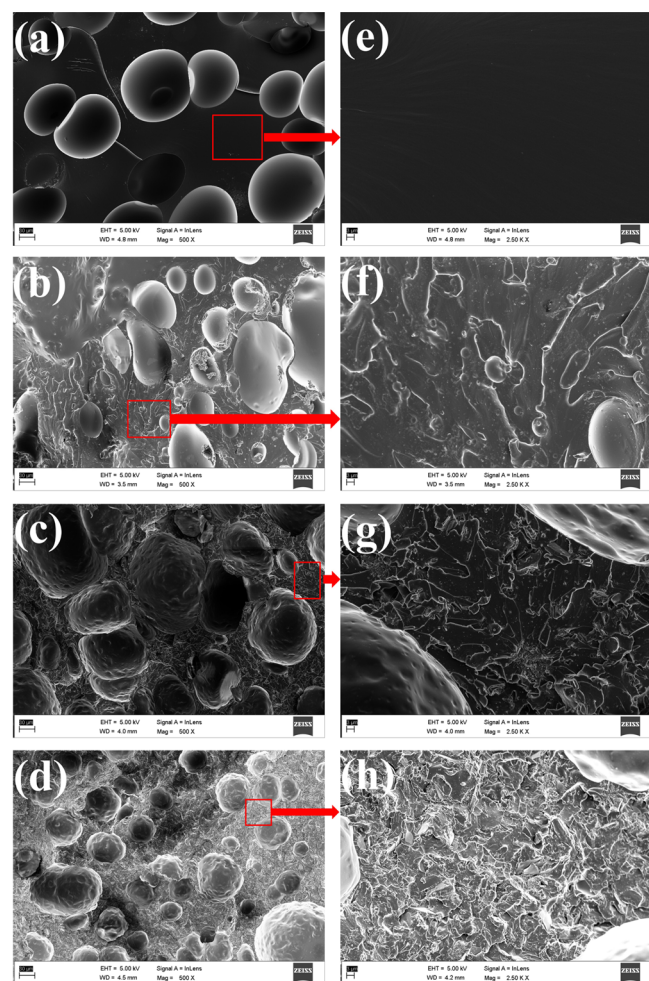
Figure 9. Typical FESEM micrographs recorded for (a) PU, (b) 1 wt %, (c) 10 wt %, and (d) 25 wt % GNCs incorporated in PU. The rectangle coupled to the arrow indicates the respective magnified regions showed in images e−h.

samples (left panel) and magnified region (right panel). One can see that the surface morphology of PU is distinctly different as compared to the morphology of GNCs incorporated in PU. In PU, uncorrugated zones are observed along with the microvoids that, inherently, exist in the host matrix. The origin of such microvoids lies in the synthesis route of PU. They were formed by onset hot press curing of the samples. The curing could be generated out-diffusion of gaseous species responsible for forming such microvoids. The size of the voids seems to be randomly distributed. Moreover, the shape is mostly spherical, and a few were found to be elliptically shaped. They are coupled to each other and thought to be formed due to local fugacity and rehology of the PU matrix. The typical magnified portion indicated (Figure 9e) homogeneous morphology of the host matrix surrounded by the microvoids (Figure 9a). The incorporation of low weight percent GNCs, such as 1, subsequently changed the morphology of the homogeneous portion of the matrix, as seen in Figure 9b,f. The uncorrugated zones in PU got embedded with the GNCs flakes, including microvoids. At this level of concentration, the amount of GNCs seems to be insufficient to get distributed uniformly. However, the coverage of GNCs on microvoids gets more dense as their weight percent in PU is increased, subsequently.

Interface Polarization Mechanism. The interface polar-ization mechanism is proposed based on the analysis of microwave scattering parameters. It indicates that the amount of orientational polarization (OP, radical) sites, atomic polarization (AP) constituents, and number of electron donor (EP) moieties available are identical in quantity. The polarization due to charge accumulation remains constant, leading to a nearly constant real permittivity value over the measured frequency range for any sample. PU consists of three shallow relaxation processes at ∼12 (EP), ∼10 (AP), and ∼9 (OP) GHz. The OP is vanishing after GNCs loading and consistent with the discussions presented on vibration spec-troscopy. It indicated that radical sites via GNCs hydrosorption are saturated. For the 12 GHz peak associated with EP, at low GNCs fraction (up to ∼5 wt %) the peak is found to have disappeared. Importantly this loading region is estimated as the percolation threshold, where efficient dispersion is speculated, as discussed in the σ_{dc} section. But thereafter emergence of the loss peak at high GNCs concentration indicates that, subsequent loading does not commensurate the amount of EP. The EP is attributed to, respectively, doubly bonded oxygen (C=O, -C=N=O-) and nitrogen (-C=N-) sites. The AP (∼10 GHz), associated with segmental motion of PU, i.e.,
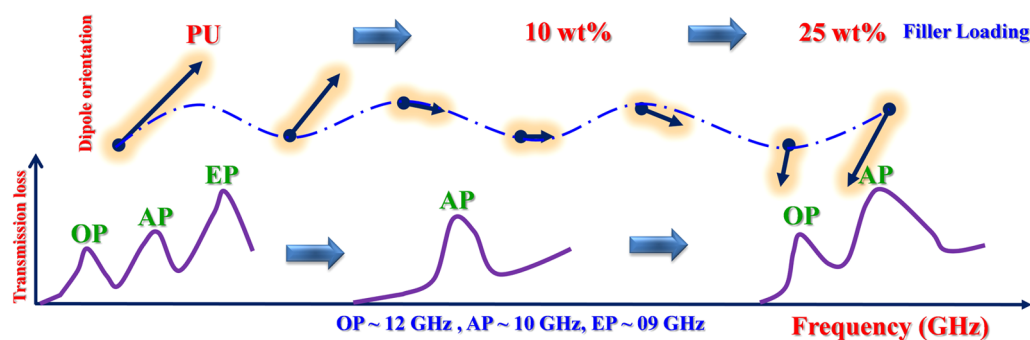
Figure 10. Scheme of interface polarization and variable contribution of polarization modes in PU and GNCs/PU nanocomposites. (OP, radical polarization associated with stereo regular -GNCs-H mode; AP, atomic polarization (urethane amide III δ(CH), at ∼1315 cm^{-1}, -N−H- at ∼1500 cm^{-1}); EP, electronic polarization indicating doubly bonded oxygen (C=O, -C=N=O-) and nitrogen (-C=N-) sites.
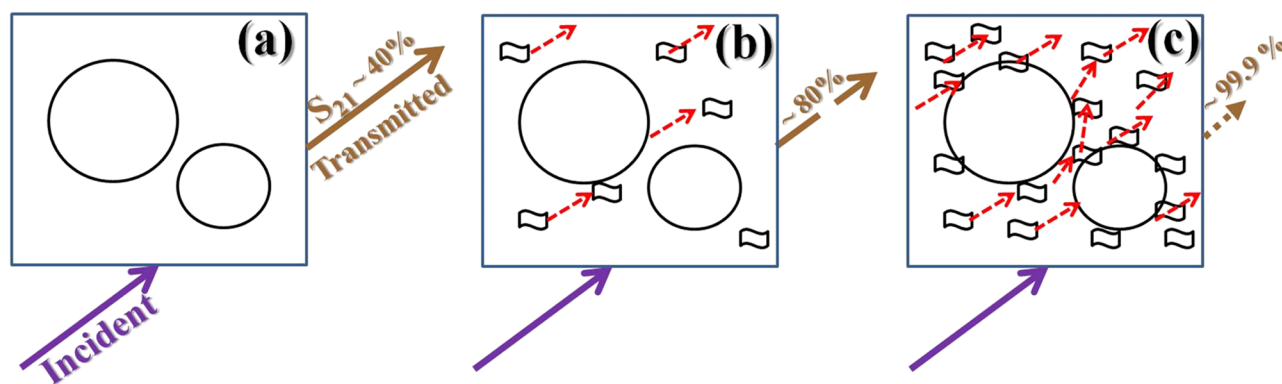
Figure 11. Schematic representation indicating the role of GNCs (hollow rectangles, b and c) in PU to enhance shielding effectiveness. The coupling of the incident electromagnetic field wiggles to the matrix that could generate a variable strength conducting path (shown by small dashed arrows). The arrows at the bottom indicate incident radiation, whereas the broken arrows at right (brown) indicate transmitted power, S_{21}, and the number shows the computed transmission loss in percent. Panel a shows hollow spheres as microvoids in PU, b shows low weight percent GNCs in the host matrix, and c shows high weight percent GNCs showing the entire coverage of GNCs on the microvoids. The strength of the conducting path is high, which leads to effective dissipation of field wiggles at higher GNCs loading.

urethane amide III δ(CH) (at ~1315 cm^{-1}) and -N−H- (1500 cm^{-1}), acts as a backbone and remains invariant even after GNCs loading. Figure 10 shows the corresponding interface polarization scheme. The estimated characteristic relaxation time $\tau_{r,OP}$ ∼ 60 fs for radically stereoregular -GNCs-H modes, whereas the magnitude of $\tau_{r,AP}$, related to segmental dynamics in the host matrix, ∼ 50 fs, and $\tau_{r,EP}$ ∼ 40 fs.

At low weight fraction up to ∼5 wt %, $\tau_{r,OP}$ and $\tau_{r,EP}$ are absent. The absence of these relaxation processes is associated with the aggregates and their interface, where polarization probably occurs within aggregates or at the periphery. Their absence, typically below the percolation threshold, indicates that the degree of dispersion of GNCs in PU is homogeneous at this weight composition. Hence characteristic relaxation, for polarized moieties, occurs via mostly AP. This resembles with σ_{dc} data analyzed for the samples. Typically below the percolation threshold, value of σ_{dc} is in the range of 10^{-12}−10^{-13} S/m having activation energy ∼ 94 meV of charge carriers pertaining to AP. However, as the filler concentration goes beyond the threshold value, dipole and electronic contributions emerge having respectively activation energies ∼ 93 and 95 meV.

Thus, the gradual enhancement of the GNCs in the PU provides the conducting path to the incident electromagnetic field to get coupled to the host matrix via generating polarization currents as shown in Figure 11, schematically. Figure 11a shows the PU matrix having microvoids in which the incident field (shown by an arrow at the bottom) almost penetrates the PU medium, having small transmission loss ∼ 40%, whereas the incorporation of GNCs at low percent, although they increase transmission loss by double ∼80%, however, are not capable of providing an effective conducting path (Figure 11b). At higher weight percent, such as more than 20 wt %, the transmission loss almost reached 99.9% (Figure 11c). This indicates that the transmission is hindered severely due to dissipation of the wiggling field into the surface by generating a polarization current assisted by GNCs. This is consistent with discussion presented earlier. The analysis presented revealed that the existence of OP and EP could be attributed to polarization associated with the homogeneous distribution of GNCs in the host matrix and around the interface of the microstructures.

4. CONCLUSIONS

The electromagnetic shielding parameters for GNCs/PU nanocomposites were studied at variable 1−25 wt % GNCs, over the 8.2−12.4 GHz regime. The focus of the discussion is, how much is the transparency of the composite material to the incident signal? The analysis of microwave scattering data provided basic insight into the behavior of the microwave field in heterogeneous composite medium. The nonplanar C−H, N−H, and C=O of PU played a decisive role in modifying dc and ac conducting properties by getting hydrosorped with sp^3 C−H sites of GNCs. The percolation threshold obtained ∼5 wt % in good agreement with the reported literature[35] and indicative of a superior degree of dispersion of GNCs. The active modes of polarization in the host are modified by GNCs, especially at the microvoid skin. The atomic mode associated with C−H and N−H, invariantly, acts as a backbone for in-plane charge transfer polarization. The characteristic relaxation time obtained and activation energy computed for the modes support our findings. The mechanism suggests loaded GNCs provide a lateral conducting path to the incident field wiggles by generating mobile charge carriers along the urethane amide III segments, around the microvoids. The coupling occurs via various modes of polarization resulting in dramatic enhancement in transmission loss. The loss improves, for PU, from ∼40 to 99.9% with reduction in coating thickness from a centimeter scale down to millimeter, at 25 wt % loading of GNCs. The GNCs/PU nanocomposites are promising for building shielding patterns, especially, at short range projectile tracking.

■ ASSOCIATED CONTENT

⑤ Supporting Information

Description of production steps involved in fabrication of torroidal shape nanocomposites and of the CAD design and photograph of the die, typical batch processing method and photograph of intermediate stages, description of adiabatic hot press molding for nanocomposites fabrication and for sample finishing such as cutting and edge polishing, and a batch photograph. The Supporting Information is available free of charge on the ACS Publications website at DOI: 10.1021/acsami.5b03122.

■ AUTHOR INFORMATION

Corresponding Author
*E-mail: prashantalegaonkar@diat.ac.in. Phone: +91-20-24304401.

Notes
The authors declare no competing financial interest.

■ REFERENCES

(1) Saville, P. *Review of Radar Absorbing Materials*; Defense Research and Development Canada: Ottawa, Canada, 2005

(2) Emerson, W. Electromagnetic Wave Absorbers and Anechoic Chambers through the Years. *IEEE Trans. Antennas Propag.* **1973**, *21*, 484−490.

(3) Yang, Y.; Gupta, M. C.; Dudley, K. L.; Lawrence, R. W. A Comparative Study of EMI Shielding Properties of Carbon Nanofiber and Multi-Walled Carbon Nanotube Filled Polymer Composites. *J. Nanosci. Nanotechnol.* **2005**, *5*, 927−931.

(4) Kuzhir, P. P.; Paddubskaya, A. G.; Shuba, M. V.; Maksimenko, S. A.; Bellucci, S. Electromagnetic Shielding Efficiency in Ka-band: Carbon Foam Versus Epoxy/Carbon Nanotube Composites. *J. Nanophotonics* **2012**, *6*, No. 061715.

(5) Rohini, R.; Bose, S. Electromagnetic Interference Shielding Materials Derived from Gelation of Multiwall Carbon Nanotubes in Polystyrene/Poly(methyl methacrylate) Blends. *ACS Appl. Mater. Interfaces* **2014**, *6*, 11302−11310.

(6) Maiti, S.; Shrivastava, N. K.; Suin, S.; Khatua, B. Polystyrene/MWCNT/Graphite Nanoplate Nanocomposites: Efficient Electromagnetic Interference Shielding Material through Graphite Nanoplate−MWCNT−Graphite Nanoplate Networking. *ACS Appl. Mater. Interfaces* **2013**, *5*, 4712−4724.

(7) Rath, S. K.; Dubey, S.; Kumar, G. S.; Kumar, S.; Patra, A.; Bahadur, J.; Singh, A.; Harikrishnan, G.; Patro, T. U. Multi-Walled CNT-Induced Phase Behaviour of Poly (Vinylidene Fluoride) and Its Electro-mechanical Properties. *J. Mater. Sci.* **2014**, *49*, 103−113.

(8) Singh, A. Carbon Nanotubes Based Nanocomposite for Electromagnetic Wave Absorption and Dynamic Structural Strain Sensing. *Indian J. Pure Appl. Phys.* **2013**, *51*, 439−443.

(9) Park, S.-H.; Theilmann, P. T.; Asbeck, P. M.; Bandaru, P. R. Enhanced Electromagnetic Interference Shielding Through the Use of Functionalized Carbon-Nanotube-Reactive Polymer Composites. *IEEE Trans. Nanotechnol.* **2010**, *9*, 464−469.

(10) Al-Saleh, M. H.; Saadeh, W. H.; Sundararaj, U. EMI Shielding Effectiveness of Carbon Based Nanostructured Polymeric Materials: A Comparative Study. *Carbon* **2013**, *60*, 146−156.

(11) Arjmand, M.; Apperley, T.; Okoniewski, M.; Sundararaj, U. Comparative Study of Electromagnetic Interference Shielding Properties of Injection Molded Versus Compression Molded Multi-Walled Carbon Nanotube/Polystyrene Composites. *Carbon* **2012**, *50*, 5126−5134.

(12) Yang, Y.; Gupta, M. C.; Dudley, K. L.; Lawrence, R. W. Novel Carbon Nanotube-Polystyrene Foam Composites for Electromagnetic Interference Shielding. *Nano Lett.* **2005**, *5*, 2131−2134.

(13) Kumar, R.; Dhakate, S. R.; Gupta, T.; Saini, P.; Singh, B. P.; Mathur, R. B. Effective Improvement of the Properties of Light Weight Carbon Foam by Decoration with Multi-Wall Carbon Nanotubes. *J. Mater. Chem. A* **2013**, *1*, 5727−5735.

(14) Yuan, B.; Yu, L.; Sheng, L.; An, K.; Zhao, X. Comparison of Electromagnetic Interference Shielding Properties between Single-Wall Carbon Nanotube and Graphene Sheet/Polyaniline Composites. *J. Phys. D: Appl. Phys.* **2012**, *45*, No. 235108.

(15) Liu, Z.; Bai, G.; Huang, Y.; Ma, Y.; Du, F.; Li, F.; Guo, T.; Chen, Y. Reflection and Absorption Contributions to the Electromagnetic Interference Shielding of Single-Walled Carbon Nanotube/Polyurethane Composites. *Carbon* **2007**, *45*, 821−827.

(16) Huang, Y.; Li, N.; Ma, Y.; Du, F.; Li, F.; He, X.; Lin, X.; Gao, H.; Chen, Y. The Influence of Single-Walled Carbon Nanotube Structure on the Electromagnetic Interference Shielding Efficiency of its Epoxy Composites. *Carbon* **2007**, *45*, 1614−1621.

(17) Kuilla, T.; Bhadra, S.; Yao, D.; Kim, N. H.; Bose, S.; Lee, J. H. Recent Advances in Graphene Based Polymer Composites. *Prog. Polym. Sci.* **2010**, *35*, 1350−1375.

(18) Singh, V. K.; Shukla, A.; Patra, M. K.; Saini, L.; Jani, R. K.; Vadera, S. R.; Kumar, N. Microwave Absorbing Properties of a Thermally Reduced Graphene Oxide/Nitrile Butadiene Rubber Composite. *Carbon* **2012**, *50*, 2202−2208.

(19) Liang, J.; Wang, Y.; Huang, Y.; Ma, Y.; Liu, Z.; Cai, J.; Zhang, C.; Gao, H.; Chen, Y. Electromagnetic Interference Shielding of Graphene/Epoxy Composites. *Carbon* **2009**, *47*, 922−925.

(20) Eswaraiah, V.; Sankaranarayanan, V.; Ramaprabhu, S. Functionalized Graphene−PVDF Foam Composites for EMI Shielding. *Macromol. Mater. Eng.* **2011**, *296*, 894−898.

(21) Chen, Z.; Xu, C.; Ma, C.; Ren, W.; Cheng, H.-M. Lightweight and Flexible Graphene Foam Composites for High-Performance Electromagnetic Interference Shielding. *Adv. Mater.* **2013**, *25*, 1296−1300.

(22) Zhang, H.-B.; Yan, Q.; Zheng, W.-G.; He, Z.; Yu, Z.-Z. Tough Graphene−Polymer Microcellular Foams for Electromagnetic Interference Shielding. *ACS Appl. Mater. Interfaces* **2011**, *3*, 918−924.

(23) Basavaraja, C.; Kim, W. J.; Do Kim, Y.; Do, S. H. Synthesis of Polyaniline-Gold/Graphene Oxide Composite and Microwave Absorption Characteristics of the Composite Films. *Mater. Lett.* **2011**, *65*, 3120−3123.

(24) Al-Saleh, M. H.; Sundararaj, U. X-Band EMI Shielding Mechanisms and Shielding Effectiveness of High Structure Carbon Black/Polypropylene Composites. *J. Phys. D: Appl. Phys.* **2013**, *46*, No. 035304.

(25) Kumar, A.; Patil, S.; Joshi, A.; Bhoraskar, V.; Datar, S.; Alegaonkar, P. Mixed Phase, sp^2-sp^3 Bonded, and Disordered Few Layer Graphene-Like Nanocarbon: Synthesis and Characterizations. *Appl. Surf. Sci.* **2013**, *271*, 86−92.

(26) *PAN Microwave Network Analyzer, Catalogue and Product Note E8364B*; Agilent: Santa Clara, CA, USA, 2009.

(27) Larkin, P. *Infrared and Raman Spectroscopy: Principles and Spectral Interpretation*; Elsevier: Amsterdam, 2011.

(28) Stuart, B. *Infrared Spectroscopy*; Wiley: Hoboken, NJ, USA, 2005.

(29) Stauffer, D.; Aharony, A. *Introduction to Percolation Theory*; CRC Press: Boca Raton, FL, USA, 1994.

(30) Obukhov, S. First Order Rigidity Transition in Random Rod Networks. *Phys. Rev. Lett.* **1995**, *74*, No. 4472.

(31) Regev, O.; ElKati, P. N.; Loos, J.; Koning, C. E. Preparation of Conductive Nanotube−Polymer Composites Using Latex Technology. *Adv. Mater.* **2004**, *16*, 248−251.

(32) Ounaies, Z.; Park, C.; Wise, K.; Siochi, E.; Harrison, J. Electrical Properties of Single Wall Carbon Nanotube Reinforced Polyimide Composites. *Compos. Sci. Technol.* **2003**, *63*, 1637−1646.

(33) Sandler, J.; Kirk, J.; Kinloch, I.; Shaffer, M.; Windle, A. Ultra-Low Electrical Percolation Threshold in Carbon-Nanotube-Epoxy Composites. *Polymer* **2003**, *44*, 5893−5899.

(34) Jonscher, A. *Dielectric Relaxation in Solids*; Chelsea Dielectrics Press: London, 1983.

(35) Li, N.; Huang, Y.; Du, F.; He, X.; Lin, X.; Gao, H.; Ma, Y.; Li, F.; Chen, Y.; Eklund, P. C. Electromagnetic Interference (EMI) Shielding of Single-Walled Carbon Nanotube Epoxy Composites. *Nano Lett.* **2006**, *6*, 1141−1145.